Rare Met. (2021) 40(2):374–382
https://doi.org/10.1007/s12598-020-01444-y

RARE METALS
www.editorialmanager.com/rmet

A nanostructured Ni/T-Nb_2O_5@carbon nanofibers as a long-life anode material for lithium-ion batteries

Si-Ru He, Jian-Peng Zou, Li-Bao Chen*, Yue-Jiao Chen*

Received: 20 February 2020 / Revised: 23 April 2020 / Accepted: 28 April 2020 / Published online: 29 May 2020

Abstract \In this work, nickel/T-Nb_2O_5 nanoparticles encapsulated in mesoporous carbon nanofibers (denoted as Ni/T-Nb_2O_5@CNFs) are successfully prepared through a simple electrospinning route and succedent heating treatment. The presence of Ni in carbon nanofibers is beneficial for enhancing the electronic conductivity and the initial Coulombic efficiency. Ni/T-Nb_2O_5 nanoparticles are homogeneously incorporated in carbon nanofibers to form a nanocomposite system, which provides effective buffering during the lithiation/delithiation process for cycling stability. The Ni/T-Nb_2O_5@CNFs show high surface area (26.321 $m^2 \cdot g^{-1}$) and mesoporous microstructure, resulting in higher capacity and excellent rate performance. The Ni/T-Nb_2O_5@CNFs exhibit a remarkable capacity of 437 $mAh \cdot g^{-1}$ at a current density of 0.5 $A \cdot g^{-1}$ after 230 cycles and a capacity of 173 $mAh \cdot g^{-1}$ at a current density up to 10.0 $A \cdot g^{-1}$ after 1400 cycles. This work indicates that nickel/T-Nb_2O_5 nanoparticles encapsulated in carbon nanofibers can be a promising candidate for anode material in high-power LIBs.

Keywords Electrospinning; Nickel; T-Nb_2O_5; Nanofiber anode; Lithium-ion batteries

1 Introduction

Lithium-ion batteries (LIBs) have been widely used as energy storage devices due to their high energy density, low cost, environmental friendliness and long life cycle [1]. However, the energy density of LIBs is seriously limited due to the low theoretical capacity of graphite anodes (372 $mAh \cdot g^{-1}$) [2, 3]. To address the problems, many efforts have been made to explore suitable anode electrode candidates for LIBs. Transition metal oxides such as Co_3O_4 [4], NiO [5] and CuO [6] have been extensively researched as anode materials due to their high availability, low cost, high theoretical capacity and their high oxidation states. Unfortunately, most of the oxides usually produce a huge volume change during the Li^+ insertion and extraction process, which leads to a rapid reduction in capacity. Additionally, Nb_2O_5 has received considerable attention as an electrode material for LIBs due to its advantageous properties, including its low but safe voltage window, multiple redox couples (Nb^{5+}/Nb^{4+}, Nb^{4+}/Nb^{3+}) and low volume expansion caused by the intercalation reaction. This material exists in many crystal structures, which depend on annealing temperature and show different charge-storage abilities, including monoclinic (H-Nb_2O_5, 1100 °C), tetragonal (M-Nb_2O_5, 1000 °C), orthorhombic (T-Nb_2O_5, 600–800 °C) and pseudo-hexagonal (TT-Nb_2O_5, 500 °C) [7]. Among these structures, T-Nb_2O_5, one of the most stable structures, has been revealed to possess excellent electrochemical behaviors with "intercalation pseudocapacitance" [8], especially showing a high capacity and prominent long-cycle stability for LIBs [9, 10]. Compared with $Li_4Ti_5O_{12}$, T-Nb_2O_5 exhibits a lower working potential, ranging from 1.0 to 1.5 V, and a higher theoretical capacity of 200 $mAh \cdot g^{-1}$ [11]. Importantly, Nb_2O_5 has a sloped charge/discharge curve and does not have a flat voltage unlike $Li_4Ti_5O_{12}$ [12]. Moreover, an interplanar lattice spacing of 0.39 nm indexed to the (001) plane exists in T-Nb_2O_5, which is larger than the diameter

S.-R. He, J.-P. Zou, L.-B. Chen*, Y.-J. Chen*
State Key Laboratory of Powder Metallurgy, Central South University, Changsha 410083, China
e-mail: lbchen@csu.edu.cn

Y.-J. Chen
e-mail: cyj.strive@csu.edu.cn

of the Li ion (0.152 nm), resulting in a faster diffusion pathway and lower energy barrier for Li^+ transport and faster charge transfer compared with other active metal oxides [13]. Nevertheless, the poor electronic conductivity and low theoretical capacity of T-Nb_2O_5 significantly limit its charge/discharge performance [14].

Many research efforts have been devoted to overcoming these inherent disadvantages of T-Nb_2O_5 for improving the cycle and rate performance of LIBs. A universal method is to prepare T-Nb_2O_5 with different nanostructures to increase the surface area of electrodes and shorten the ion diffusion path, such as nanofibers and nanotubes [15, 16]. Other popular strategies are to fabricate carbon-based nanocomposites wrapped in a conductive surface coating or to fabricate porous structures to achieve high capacity, long life cycle and moderate rate capacity [15]. Additionally, the doping or substitution of various elements into the crystal lattice of electrode materials can significantly improve the conductivity and stability of electrode materials, further improving their electrochemical performance [17–20]. Recently, electrospinning has become an effective technique to fabricate fibrous carbon-based composites with diameters ranging from a few nanometers to micrometers for use in LIBs, due to its low price and simplicity [21]. Nanofibers obtained using electrospinning can significantly increase the surface areas of active materials and increase the electrical contact between material and electrolyte [22, 23]. As a result, excellent electrochemical performance can be obtained by uniformly dispersing metal oxide nanoparticles in carbon nanofibers (CNFs) [24].

In this work, nickel/T-Nb_2O_5 nanoparticles encapsulated in mesoporous carbon nanofibers (denoted as Ni/T-Nb_2O_5@CNFs) are prepared through a simple electrospinning route and succedent annealing treatment for use in LIBs. To the best of our knowledge, few previous studies on Ni/T-Nb_2O_5@CNFs have been reported. The presence of Ni in carbon nanofibers is beneficial as it provides more active sites for Li-ion diffusion, which enhances the electronic conductivity and improves the initial Coulombic efficiency [25, 26]. In this study, Ni/T-Nb_2O_5 nanoparticles are homogeneously incorporated in carbon nanofibers, thus forming a nanocomposite system. The carbon nanofibers not only serve as a conductive network to increase the conductivity of the T-Nb_2O_5, but also provide effective buffering for T-Nb_2O_5 during the lithiation/delithiation process, which is beneficial to Li-ion storage and cycling stability [27]. The results demonstrate that the nanocomposite system has a remarkable discharge capacity of up to 173 $mAh{\cdot}g^{-1}$ at a current density of 10.0 $A{\cdot}g^{-1}$ after 1400 cycles. This work demonstrates that nickel/T-Nb_2O_5 nanoparticles encapsulated in carbon nanofibers could be a promising candidate for anode material in high-power LIBs.

2 Experimental

2.1 Preparation of Ni/T-Nb_2O_5@CNFs nanostructure by electrospinning

All chemicals were applied directly without any purification. Firstly, 0.2841 g niobium oxalate ($C_{10}H_5NbO_{20}$) (Shanghai SUNHO, Shanghai, China) and 0.0650 g nickel acetate tetrahydrate ($C_4H_{14}NiO_8$) (Aladdin Industrial Corporation, Shanghai, China) were dissolved in 5 ml *N*,*N*-dimethylformamide (DMF) under magnetic stirring for 3 h at 70 °C. Secondly, 0.5819 g polyvinylpyrrolidone (PVP; relative molecular mass of M_w = 1,3000,000; Aladdin Industrial Corporation) was dissolved in the above solution and vigorously stirred for 12 h at room temperature. Electrospinning was conducted under the following conditions: flow rate of 0.4 $ml{\cdot}h^{-1}$; a distance of 25 cm between the collector and the tip of the needle (25 gauge); and an applied voltage of 15 kV. The as-spun fibers were calcined at 650 °C for 2.5 h with a ramping rate of 2 $°C{\cdot}min^{-1}$ under argon flow. For comparison, simple nanofibers without nickel were prepared in the same condition. The electrospinning process for CNFs is shown graphically in Fig. 1.

2.2 Characterization of materials

The crystal structure of calcined materials was analyzed by X-ray diffractometer (XRD, Rigaku D/Max 2500, Rigaku Corporation, Tokyo, Japan) using Cu Kα radiation (λ = 0.15406 nm). The morphology and structure of the materials were observed using a Nova NanoSEM 230 field emission scanning electron microscope (FESEM, FEI Company, Hillsboro, OR, USA) and a JEM-2100F high-resolution transmission electron microscope (HRTEM, JEOL Ltd., Tokyo, Japan). Additionally, the materials were analyzed using thermogravimetric analysis (TGA, WRT-11, Beiguang Hongyuan Instrument Co., LTD, China) under flowing air at a heating rate of 10 $°C{\cdot}min^{-1}$ to a final temperature of 800 °C. To measure the surface area of the

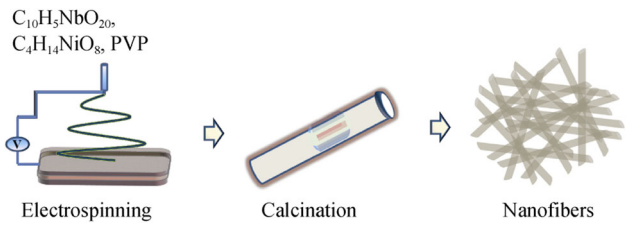

Fig. 1 Schematic illustration on electrospinning process

CNFs, Brunauer–Emmett–Teller (BET) analysis was conducted using a TriStar II 3020 device (Micromeritics Instrument Corporation, Norcross, GA, USA). The pore size distribution was determined using the Barrett–Joyner–Halenda (BJH) method. An iCAP 7400 inductively coupled plasma optical emission spectrometer (ICP-OES, Thermo Fisher Scientific, Waltham, MA, USA) was used to analyze the elemental content of the materials.

2.3 Cell assembly and electrochemical cell testing

Working electrodes were prepared using 80% active materials, 10% acetylene black and 10% polyvinylidene fluoride (PVDF) in *N*-methylpyrrolidone (NMP). The resulting slurries were cast onto a Cu foil with quality ranging from 0.35 to 0.50 $mg{\cdot}cm^{-1}$ and then dried at 120 °C for 12 h in a vacuum. Then, the resulting film was cut into disks with a diameter of 14 mm. The electrochemical properties were determined using coin cells which were assembled as GR2016 coin-type half-cells in an argon-filled glove box (M.BRAUN INERT-GAS-SYSTEME GMBH, Garching, Germany; O_2 and $H_2O < 0.1 \times 10^{-6}$) with Li metal as the counter electrode. The electrolyte was 1 $mol{\cdot}L^{-1}$ $LiPF_6$ in ethylene carbonate/ethyl methyl carbonate/propylene carbonate(EC/EMC/PC, 20/65/5 by volume) solvent and vinylene carbonate/lithium bis(fluorosulfonyl)imide (VC/LiFSI, 1.5/3, by volume) as an additive agent, and a porous polypropylene membrane (Celgard 2500, Guangdong JiuMei New Material Co., Ltd.) was used as the separator. The galvanostatic charge/discharge behaviors of cells were determined using a LANHE CT2001A battery testing system (Wuhan LAND Electronics Co., Wuhan, China) between 0.01 and 3.00 V at 30 °C. Cyclic voltammetry (CV) was measured using an Arbin LBT21024 battery testing system (Arbin Instruments, College Station, TX, USA). Electrochemical impedance spectroscopy (EIS) tests were carried out with Nyquist plots using a ZIVE SP1 battery testing device (WonATech Co., Ltd., Seoul, Korea) in order to measure the internal resistance of coin cells at frequencies of 0.01–100.00 kHz.

3 Results and discussion

XRD patterns of the as-prepared Ni/T-Nb_2O_5@CNFs are shown in Fig. 2a. The sharp diffraction peaks at 22.6°, 28.4°, 36.6° and 46.2° were ascribed to the (001), (180), (181) and (002) diffraction peaks of the T-Nb_2O_5 phase (JCPDS No. 071-0336) (lattice constants: a = 0.6175 nm, b = 2.9175 nm, c = 0.3930 nm), which is the same as that previously reported [28]. Additionally, two obvious peaks located at 44.5° and 51.8° ascribe to the (111) and (200), which belong to the metallic nickel (JCPD No. 04-0850), and no diffraction peaks of NiO were observed [29, 30]. TGA results of the as-spun precursor are shown in Fig. 2b. The decomposition of the precursor into Ni/T-Nb_2O_5@CNFs was carried out at 800 °C in air at a heating rate of 10 $°C{\cdot}min^{-1}$. The first weight loss of 12.5% before 300 °C is ascribed to the elimination of adsorbed water in the sample. When the temperature exceeds 300 °C, the rate of weight loss increases, and a weight loss of 47.4% occurs between 300 and 583 °C due to the oxidation of carbon. A weight loss observed between 583 and 630 °C is due to a phase transformation from $Nb_2O_5{\cdot}H_2O$ to Nb_2O_5 [31], which results from the disappearance of crystalline water. Based on this result, the carbon content of the precursor can be estimated to be about 47.4 wt%, which is similar to a previously reported result [32]. The results of the elemental analysis by ICP-OES show that Ni and Nb contents are 6.21 wt% and 7.72 wt%, respectively, corresponding from metallic nickel and Nb_2O_5. To quantitatively examine the surface and porosity of the Ni/T-Nb_2O_5@CNFs, nitrogen adsorption–desorption measurements were conducted. The results are shown in Fig. 2c. It can be seen that the Ni/T-Nb_2O_5@CNFs have a high surface area of 26.321 $m^2{\cdot}g^{-1}$, which is about six times that of T-Nb_2O_5CNFs (3.8 $m^2{\cdot}g^{-1}$) [33]. The corresponding pore size distribution is shown in Fig. 2d. As can be seen, the pore size ranged from 3 to 7 nm. The characteristics of the N_2 adsorption curve suggest that the average pore size of 3.8 nm corresponds to a mesoporous structure in the nanoscale interconnecting walls. Such mesoporous sites also allow better penetration of electrolyte, facilitating Li-ion diffusion [33].

The morphology of the precursor and the Ni/T-Nb_2O_5@CNFs was characterized via FESEM, as shown in Fig. 3a, b. These images indicate typical electrospun nanofibers with a diameter of about 100 nm. No obvious pore structure can be observed in the nanofibers. In Fig. 3c, TEM image shows that metallic nickel particles (white agglomerations) are evenly distributed in the nanofibers. HRTEM images and corresponding fast Fourier transform (FFT) pattern (Fig. 3d) further evidence the (001) plane and (180) plane for the orthorhombic phase of Nb_2O_5, respectively, corresponding to two lattice spacings of about 0.39 and 0.31 nm, which is consistent with XRD results. To further investigate the component distribution of Ni/T-Nb_2O_5@CNFs, elemental mapping was performed. The results shown in Fig. 3f–j prove the presence and uniform distribution of C, N, Ni, Nb and O.

The electrochemical performance of Ni/T-Nb_2O_5@CNFs and T-Nb_2O_5@CNFs in Li-ion half-cells was investigated. Figure 4a shows the results of the initial three-cycle CV curves at a scan rate of 0.1 $mV{\cdot}s^{-1}$ for the potential range of 0.01–3.00 V. From CV profiles, the redox reactions and phase changes during charge/discharge process can be inferred. The anodic and cathodic currents

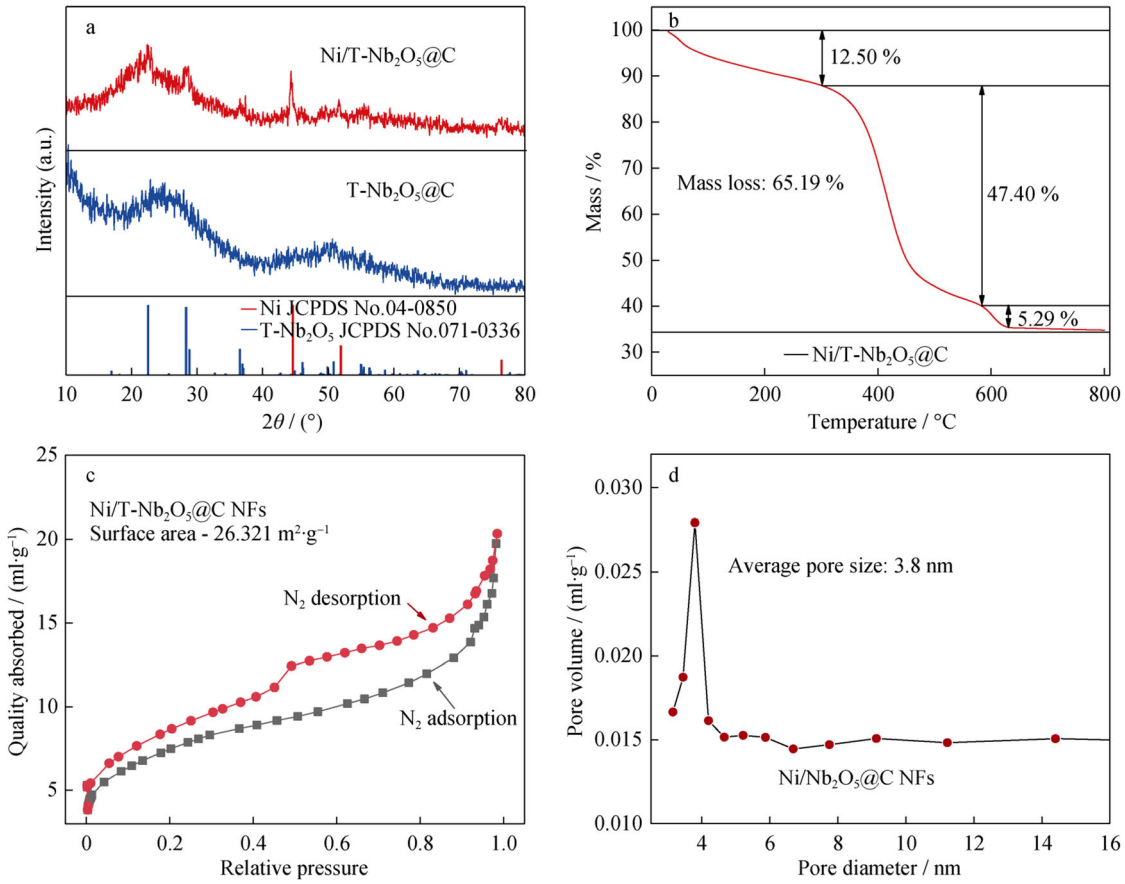

Fig. 2 **a** XRD patterns of as-prepared Ni/T-Nb_2O_5@CNFs, **b** TGA curves of Ni/T-Nb_2O_5@CNFs, **c** nitrogen adsorption–desorption isotherms for Ni/T-Nb_2O_5@CNFs, **d** pore size distribution of Ni/T-Nb_2O_5@CNFs

resulting from Li-ion insertion and extraction processes can be described as follows [34]:

$$x\,Li^+ + x\,e^- + \ Nb_2O_5 \leftrightarrow Li_xNb_2O_5 \qquad (1)$$

The inserted Li ion has a maximum x value of 2 (mole fraction) for crystalline Nb_2O_5 [33]. In the negative scan process, the broad peak region from 1.0 to 1.5 V reflects the formation of solid electrolyte interphase (SEI) at the electrode–electrolyte interface and irreversible Li-ion intercalation. The small peaks in the second and third cycle at 1.78 and 1.55 V, respectively, correspond to the reduction reaction of Nb^{5+}/Nb^{4+} couples [35]. Moreover, the broad peaks in the first cycle at 1.43 and 1.25 V, respectively, are due to the reduction reaction of Nb^{4+}/Nb^{3+} couples [36]. In the positive scan process, the broad peak ranging from 0.75 to 1.50 V can be ascribed to the oxidation reaction of Nb^{3+}/Nb^{4+} and Nb^{4+}/Nb^{5+} couple, suggesting Li-ion de-intercalation from Nb_2O_5. Previous authors attributed the peak at 2.8 V to the reaction between Li-ion and copper oxide layer current collector [37].

Figure 4b shows the charge/discharge curve of the Ni/T-Nb_2O_5@CNFs at a current density of 0.2 $A{\cdot}g^{-1}$ in the first cycle in the voltage range of 0.01–3.00 V versus Li^+/Li. The charge/discharge curve shows that potential changes proceeding is well matched with CV shapes, with an initial charge capacity and discharge capacity of 980.42 and 642.7 $mAh{\cdot}g^{-1}$, respectively, revealing an initial Coulombic efficiency (CE) of 65.71%. This low CE is attributed to the formation of SEI with the decomposition of electrolyte and the irreversible capacity of the electrode [33]. Meanwhile, the large pore volume increases the number of ion storage sites and access for electrolyte penetration. A comparison of the discharge capacity of the Ni/T-Nb_2O_5@CNFs with those of nickel-free CNFs at different current densities is shown in Fig. 4c. It can be seen that Ni/T-Nb_2O_5@CNFs had better electrochemical performance at higher current densities. At a current density of 10.0 $A{\cdot}g^{-1}$, Ni/T-Nb_2O_5@CNFs exhibited a capacity of 227 $mAh{\cdot}g^{-1}$, while nickel-free T-Nb_2O_5@CNFs exhibited a capacity of about 50 $mAh{\cdot}g^{-1}$. Therefore, the Ni/T-Nb_2O_5@CNFs have a superior rate performance than nickel-free T-Nb_2O_5@CNFs T-Nb_2O_5. Figure 4d shows a schematic diagram of nickel uniformly dispersed in nanofibers, indicating that the addition of nickel increases the electron transfer. Figure 4e displays the long-term cycling

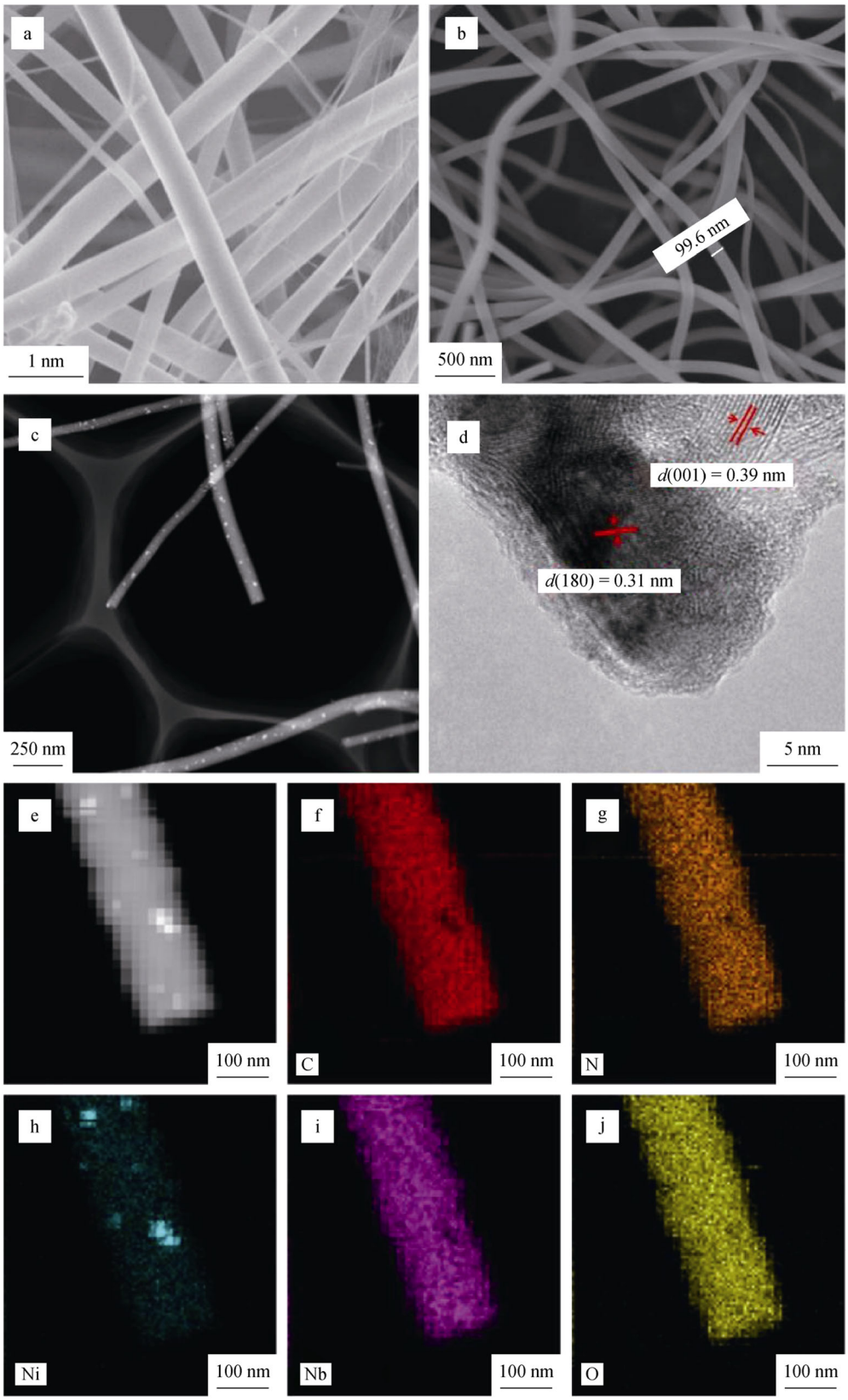

Fig. 3 **a**, **b** SEM images of precursor and as-prepared Ni/T-Nb_2O_5@CNFs, **c** HRTEM image of Ni/T-Nb_2O_5@CNFs, **d** crystal plane labeling of Ni/T-Nb_2O_5@CNFs, **e** selected area of Ni/T-Nb_2O_5@CNFs used in elemental mapping images in following panels; elemental mapping images of Ni/T-Nb_2O_5@CNFs: **f** C, **g** N, **h** Ni, **i** Nb and **j** O

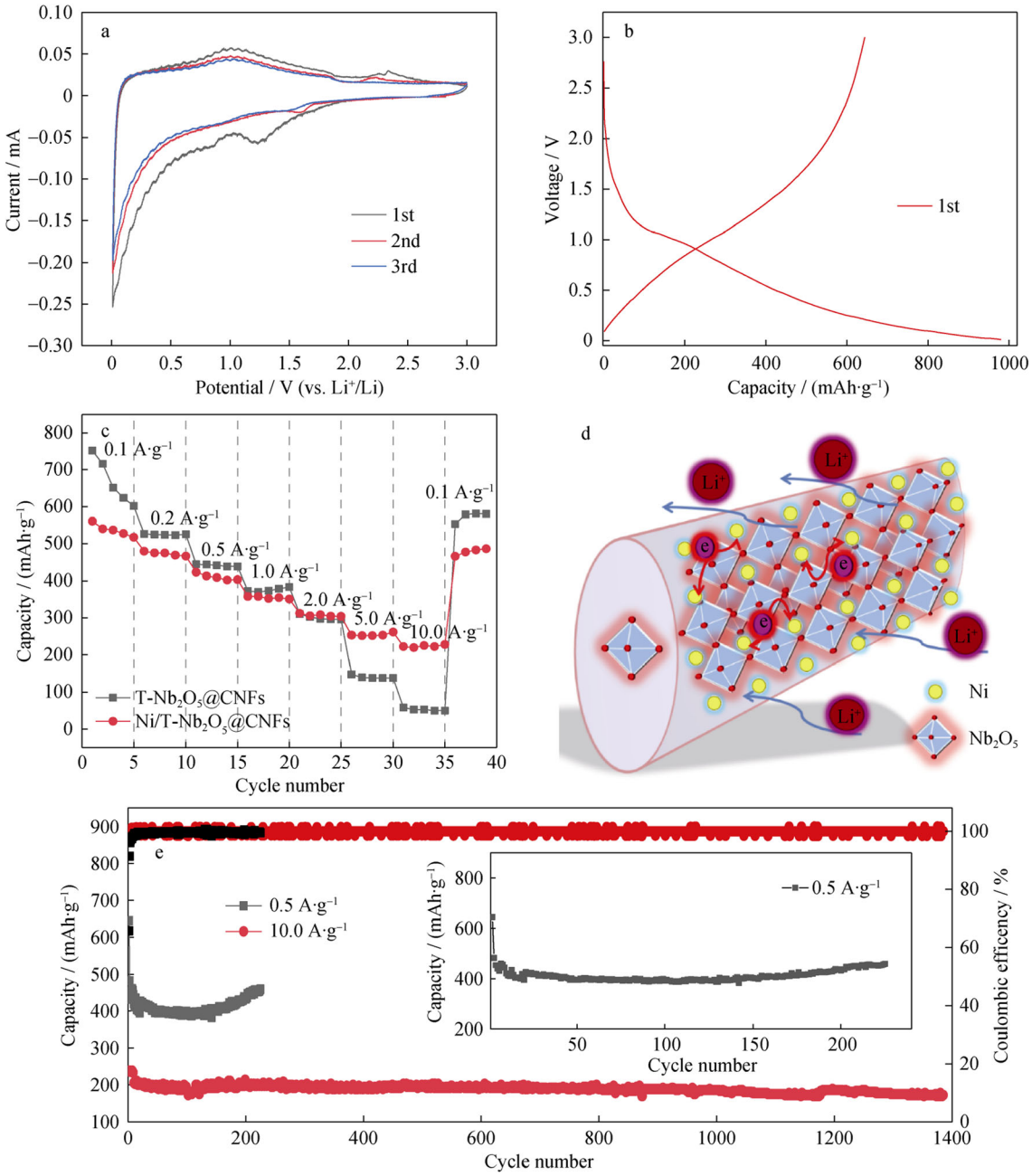

Fig. 4 **a** First three cycles of CV profiles of Ni/T-Nb_2O_5@CNFs at a scan rate of 0.1 mV·s^{-1}, **b** galvanostatic charge/discharge curves for the first cycles, **c** rate capacity of Ni/T-Nb_2O_5@CNFs and T-Nb_2O_5@CNFs at different current densities, **d** graphical illustration of how nickel improves electronic transmission and Li-ion charge transport, **e** capacity retention characteristics of Ni/T-Nb_2O_5@CNFs for 1400 cycles at a current density of 10 A·g^{-1}

performance of Ni/T-Nb_2O_5@C NFs electrode at 10.0 A·g^{-1}, and it exhibits a reversible charge capacity of about 173 mAh·g^{-1} after 1400 cycles and shows a reversible capacity of 437 mAh·g^{-1} after 230 cycles at 0.5 A·g^{-1}. (Detailed explanation shows in inset of Fig. 4e.)

In order to investigate the pseudocapacitive feature of Ni/T-Nb_2O_5@CNFs, CV was measured at different sweep rates from 0.1 to 5.0 mV·s^{-1} in the voltage range of 0.01–3.00 V (Fig. 5a). In general, the electrochemical specific capacity can be separated into three parts: (1) pseudocapacitance, (2) non-Faradaic contribution from the double-layer effect and (3) the Faradaic contribution from the Li-ion intercalation process. The change in the peak current (I) and the scan rate (v) corresponds to a different storage process [38]:

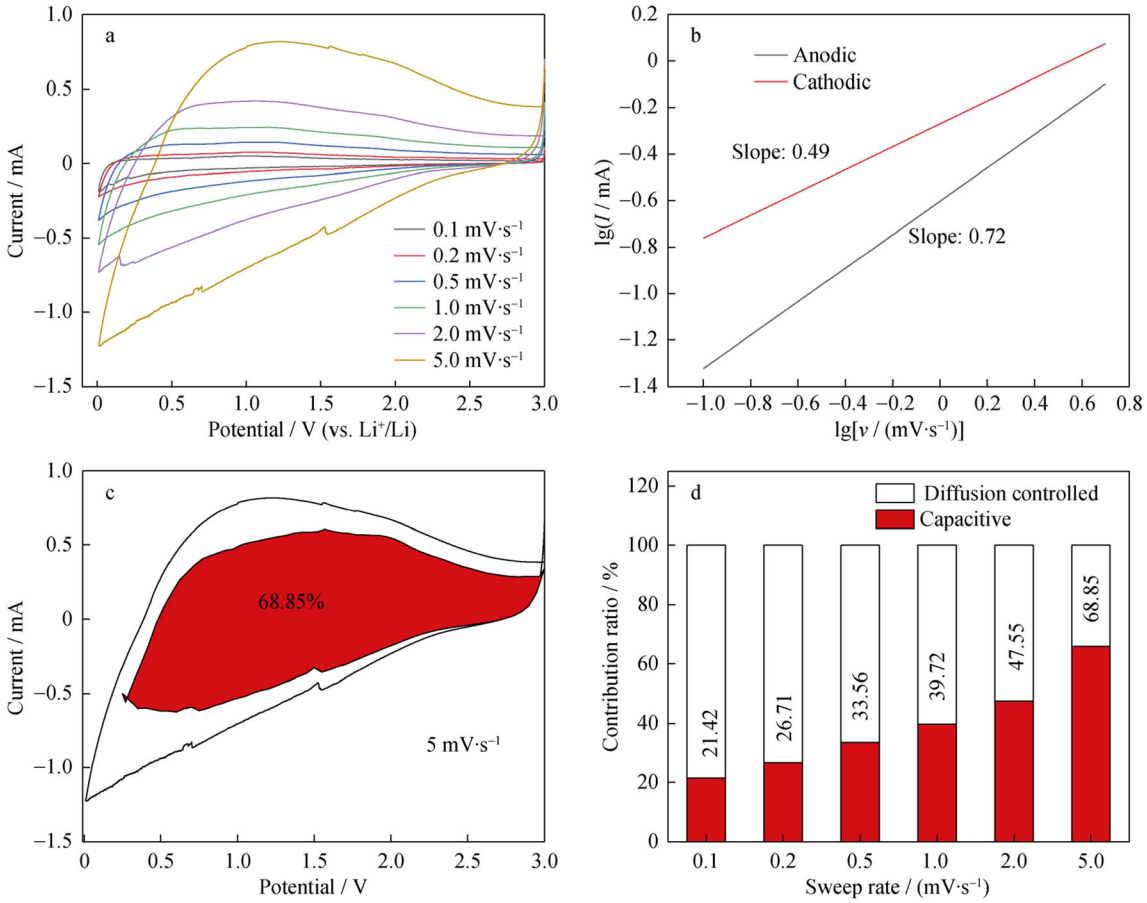

Fig. 5 Results of kinetic analysis of Li^+ intercalation behavior of Ni/T-Nb_2O_5@CNFs: **a** CV curves of Ni/T-Nb_2O_5@CNFs at different scan rates, **b** relationship between lg$I$ (where I is current) and lg$v$ (where v is sweep rate) used to determine values of b, **c** separation between capacitive current and diffusion current in Ni/T-Nb_2O_5@CNFs at a scan rate of 5 mV·s^{-1}, **d** pseudocapacitive contribution ratio of Ni/T-Nb_2O_5@CNFs at different scan rates

$$I = av^b \tag{2}$$

$$I = k_1 + k_2 v^{1/2} \tag{3}$$

where a and b are adjustable parameters, and k_1 can be determined from the slope by plotting $v^{1/2}$ against $i/v^{1/2}$. The b value can be used to qualitatively distinguish the proportion of the surface redox capacitive part and diffusion intercalation part. When the value of b is about 0.5, it indicates that the Li-ion intercalation process plays a leading role in materials, whereas when the value of b is near 1, it indicates that the capacitive process caused by surface effects. Figure 5b demonstrates that the values of b are 0.72 and 0.49 for anodic and cathodic peaks, respectively, at sweep rates in the range of 0.1–5.0 mV·s^{-1}. Figure 5c shows the diffusion current and separation of the capacitive current in the Ni/T-Nb_2O_5@CNFs at a scan rate of 5 mV·s^{-1}. It indicates that a high proportion of the capacity of Ni/T-Nb_2O_5@CNFs is provided by the surface redox mechanism, signifying that a higher discharge capacity arises on the surface of the CNFs. Figure 5d shows the calculated contribution of pseudocapacitive charge to the capacitive process with sweep rate changing; the pseudocapacitive contribution increases from 21.42% to 68.85% as the sweep rate increases from 0.1 to 5.0 mV·s^{-1}. Furthermore, the explanations for the outstanding electrochemical performances of the Ni-doped T-Nb_2O_5@CNFs for LIBs include: (1) The idiographic nanostructure created by electrospinning can shorten Li-ion and electron diffusion routes, which allows rapid charge transport, and the high surface area provides more reactive sites during the cycles; and (2) the introduction of metallic nickel provides a conductive network, which increases electron transport.

Figure 6a shows EIS curves of Ni/T-Nb_2O_5@CNFs, T-Nb_2O_5@CNFs and Ni/T-Nb_2O_5@CNFs after 1400 cycles. The curve has a semicircular shape in the high-frequency region, corresponding to the resistance to charge transfer in the surface of the active material, and presents an inclined line in the low-frequency region, which indicates the diffusion of Li ions in the electrode. And it can be

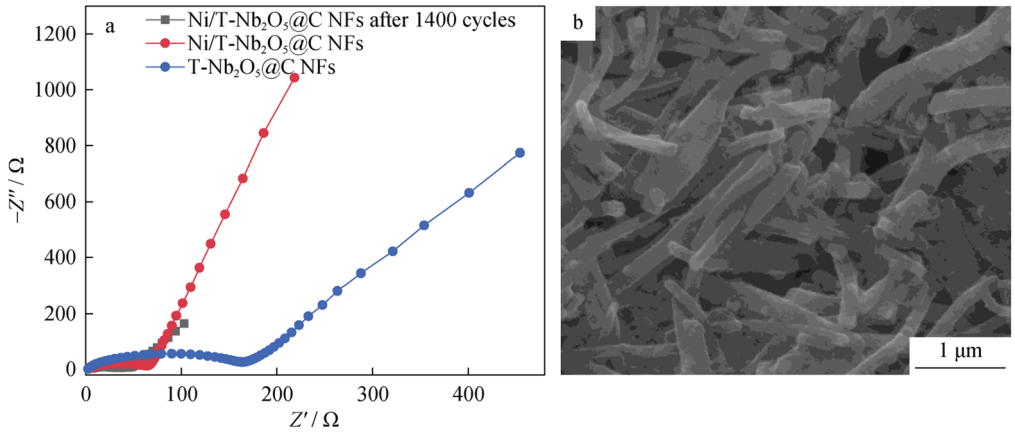

Fig. 6 **a** EIS spectra of pristine Ni/T-Nb_2O_5@CNFs, T-Nb_2O_5@CNFs and Ni/T-Nb_2O_5@CNFs after 1400 cycles, where Z' is the real part of impedance and Z'' is the imaginary part of impedance, **b** SEM image of Ni/T-Nb_2O_5@CNFs after 1400 cycles

Table 1 Previously reported electrochemical behaviors of different Nb_2O_5-based materials used as anode Li-ion batteries

Electrode materials	Capacity/ ($mAh·g^{-1}$)	Number of cycles	Current density/($A·g^{-1}$)	Rate capacity/ ($mAh·g^{-1}$)	Current density/($A·g^{-1}$)	Voltage range/V	References
3DOM T-Nb_2O_5	124	100	2.00	106	4.0	1.00–3.00	[28]
Nb_2O_5 nanospheres	404.6	100	0.04	345.5	0.4	0.01–2.00	[14]
Nano-Nb_2O_5 powder	143	800	0.50	43	10.0	0.05–3.00	[8]
Nb_2O_5 nanofibers	160	2000	0.50	70	5.0	1.00–2.50	[1]
Nb_2O_5/C composites	150	100	0.50	160	1.0	0.01–3.00	[39]
Ni/Nb_2O_5@CNFs	173	1400	10.00	227	10	0.01–3.00	This work

seen that the charge transfer resistance of Ni/T-Nb_2O_5@CNFs is much lower than that of the pure T-Nb_2O_5@CNFs. Additionally, no morphological collapse was observed after 1400 cycles, as shown in Fig. 6b, which reveals the long cycling stability of Ni/T-Nb_2O_5@CNFs (Fig. 5e).

Table 1 summarizes previous reports of the electrochemical behaviors of Nb_2O_5-based anode material for LIBs. Nano-Nb_2O_5 powder delivered a long cycling stability, maintaining a capacity of 143 $mAh·g^{-1}$ at 0.5 $A·g^{-1}$ after 800 cycles [10]; however, the capacity was only 43 $mAh·g^{-1}$ at 10.0 $A·g^{-1}$ after 800 cycles, showing a poor rate performance. The Ni/T-Nb_2O_5@CNFs constructed in the present study exhibited a higher capacity, higher rate capability and higher cycling stability compared with the results reported in Table 1 [1, 8, 14, 28, 39].

4 Conclusion

In summary, we have successfully fabricated Ni/T-Nb_2O_5@CNFs by electrospinning and calcination. The Ni/T-Nb_2O_5@CNFs have a high surface area (26.321 $m^2·g^{-1}$) and have nano-mesoporous sites, where Li ion and electron transport can take place, which is critical for the pseudocapacitive behavior of the CNFs. The Ni/T-Nb_2O_5@CNFs exhibit outstanding cycling stability and rate performance (a capacity of 173 $mAh·g^{-1}$ after 1400 cycles at a current density of 10.0 $A·g^{-1}$). We show that the Ni metal particles are dispersed evenly in the CNFs, which improves the conductivity of the electrode materials. We believe this work will open a new avenue for the design and application of advanced electrode materials for high rate performance and high conductivity.

Acknowledgements This research was financially supported by the National Natural Science Foundation of China (Nos. 51771236, 51901249, U1904216) and the Science Fund for Distinguished Young Scholars of Hunan Province (No. 2018JJ1038).

References

[1] Cheong JY, Jung JW, Youn DY, Kim C, Yu S, Cho SH, Yoon KR, Kim ID. Mesoporous orthorhombic Nb_2O_5 nanofibers as pseudocapacitive electrodes with ultra-stable Li storage characteristics. J Power Sources. 2017;360:434.

[2] Sun LY, Yang L, Li J, Narayan RL, Ning XH. Superior full-cell cycling and rate performance achieved by carbon coated hollow Fe_3O_4 nanoellipsoids for lithium ion battery. Electrochim Acta. 2018;288:71.

[3] Lou S, Cheng X, Zhao Y, Lushington A, Gao J, Li Q, Zuo P, Wang B, Gao Y, Ma Y, Du C, Yin G, Sun X. Superior performance of ordered macroporous $TiNb_2O_7$ anodes for lithium ion batteries: understanding from the structural and pseudocapacitive insights on achieving high rate capability. Nano Energy. 2017;34:15.
[4] Wang G, Zhu F, Xia J, Wang L, Meng Y, Zhang Y. Preparation of Co_3O_4/carbon derived from ionic liquid and its application in lithium-ion batteries. Electrochim Acta. 2017;257:138.
[5] Zheng Y, Li Y, Yao J, Huang Y, Xiao S. Facile synthesis of porous tubular NiO with considerable pseudocapacitance as high capacity and long life anode for lithium-ion batteries. Ceram Int. 2018;44(2):2568.
[6] Wang C, Higgins D, Wang F, Li D, Liu R, Xia G, Li N, Li Q, Xu H, Wu G. Controlled synthesis of micro/nanostructured CuO anodes for lithium-ion batteries. Nano Energy. 2014;9:334.
[7] Kodama R, Terada Y, Nakai I, Komaba S, Kumagai N. Electrochemical and in situ XAFS-XRD investigation of Nb_2O_5 for rechargeable lithium batteries. J Electrochem Soc. 2006;153(3): A583.
[8] Lübke M, Sumboja A, Johnson ID, Brett DJL, Shearing PR, Liu Z, Darr JA. High power nano-Nb_2O_5 negative electrodes for lithium-ion batteries. Electrochim Acta. 2016;192:363.
[9] Yang H, Xu R, Gong Y, Yao Y, Gu L, Yu Y. An interpenetrating 3D porous reticular Nb_2O_5@carbon thin film for superior sodium storage. Nano Energy. 2018;48:448.
[10] Lubimtsev AA, Kent PRC, Sumpter BG, Ganesh P. Understanding the origin of high-rate intercalation pseudocapacitance in Nb_2O_5 crystals. J Mater Chem A. 2013;1(47):14951.
[11] Come J, Augustyn V, Kim JW, Rozier P, Taberna PL, Gogotsi P, Long JW, Dunn B, Simon P. Electrochemical kinetics of nanostructured Nb_2O_5 electrodes. J Electrochem Soc. 2014; 161(5):A718.
[12] Zhu GN, Chen L, Wang YG, Wang CX, Che RC, Xia YY. Binary $Li_4Ti_5O_{12}$–$Li_2Ti_3O_7$ nanocomposite as an anode material for Li-ion batteries. Adv Funct Mater. 2013;23(5):640.
[13] Wang L, Bi X, Yang S. Partially single-crystalline mesoporous Nb_2O_5 nanosheets in between graphene for ultrafast sodium storage. Adv Mater. 2016;28(35):7672.
[14] Arunkumar P, Ashish AG, Babu B, Sarang S, Suresh A, Sharma CH, Thalakulam M, Shaijumon MM. Nb_2O_5/graphene nanocomposites for electrochemical energy storage. RSC Adv. 2015;5(74):59997.
[15] Idrees F, Cao CB, Ahmed R, Butt FK, Butt S, Tahir M, Tanveer M, Aslam I, Ali Z. Novel nano-flowers of Nb_2O_5 by template free synthesis and enhanced photocatalytic response under visible light. Sci Adv Mater. 2015;7(7):1298.
[16] Cui C, Wei Z, Zhou G, Wei W, Ma J, Chen L, Li C. Quasi-reversible conversion reaction of $CoSe_2$/nitrogen-doped carbon nanofibers towards long-lifetime anode materials for sodium-ion batteries. J Mater Chem A. 2018;6(16):7088.
[17] Bei PW, Rui L, Dong L. Preparation and electrochemical properties of Sn/C composites. Rare Met. 2019;38(10):996.
[18] Yi TF, Zhu YR, Tao W, Luo S, Xie Y, Li XF. Recent advances in the research of $MLi_2Ti_6O_{14}$ (M = 2Na, Sr, Ba, Pb) anode materials for Li-ion batteries. J Power Sources. 2018;399:26.
[19] Li X, Hu X, Zhou L, Wen R, Xu X, Chou S, Chen L, Cao A-M, Dou S. A S/N-doped high-capacity mesoporous carbon anode for Na-ion batteries. J Mater Chem A. 2019;7(19):11976.
[20] Li X, Liu T, Wang YX, Chou SL, Xu X, Cao A, Chen L. S/N-doped carbon nanofibers affording Fe_7S_8 particles with superior sodium storage. J Power Sources. 2020;451:227790.
[21] Mai L, Xu L, Han C, Xu X, Luo Y, Zhao S, Zhao Y. Electrospun ultralong hierarchical vanadium oxide nanowires with high performance for lithium ion batteries. Nano Lett. 2010;10(11): 4750.
[22] Hwang TH, Lee YM, Kong BS, Seo JS, Choi JW. Electrospun core-shell fibers for robust silicon nanoparticle-based lithium ion battery anodes. Nano Lett. 2012;12(2):802.
[23] Li X, Sun Y, Xu X, Wang YX, Chou SL, Cao A, Chen L, Dou SX. Lotus rhizome-like S/N–C with embedded WS_2 for superior sodium storage. J Mater Chem A. 2019;7(45):25932.
[24] Zhang G, Zhu J, Zeng W, Hou S, Gong F, Li F, Li CC, Duan H. Tin quantum dots embedded in nitrogen-doped carbon nanofibers as excellent anode for lithium-ion batteries. Nano Energy. 2014;9:61.
[25] Wei Y, Zheng J, Cui S, Song X, Su Y, Deng W, Wu Z, Wang X, Wang W, Rao M, Lin Y, Wang C, Amine K, Pan F. Kinetics tuning of Li-ion diffusion in layered $Li(Ni_xMn_yCo_z)O_2$. J Am Chem Soc. 2015;137(26):8364.
[26] Kang YM, Kim KT, Kim JH, Kim HS, Lee PS, Lee JY, Liu HK, Dou SX. Electrochemical properties of Co_3O_4, Ni–Co_3O_4 mixture and Ni–Co_3O_4 composite as anode materials for Li ion secondary batteries. J Power Sources. 2004;133(2):252.
[27] Zhu J, Hou J, Uliana A, Zhang Y, Tian M, van der Bruggen B. The rapid emergence of two-dimensional nanomaterials for high-performance separation membranes. J Mater Chem A. 2018;6(9):3773.
[28] Lou S, Cheng X, Wang L, Gao J, Li Q, Ma Y, Gao Y, Zuo P, Du C, Yin G. High-rate capability of three-dimensionally ordered macroporous T-Nb_2O_5 through Li^+ intercalation pseudocapacitance. J Power Sources. 2017;361:80.
[29] Ni J, Wang W, Wu C, Liang H, Maier J, Yu Y, Li L. Highly reversible and durable Na storage in niobium pentoxide through optimizing structure, composition, and nanoarchitecture. Adv Mater. 2017;29(9):1605607.
[30] Sun X, Si W, Liu X, Deng J, Xi L, Liu L, Yan C, Schmidt OG. Multifunctional Ni/NiO hybrid nanomembranes as anode materials for high-rate Li-ion batteries. Nano Energy. 2014;9: 168.
[31] Li S, Xu Q, Uchaker E, Cao X, Cao GZ. Comparison of amorphous, pseudohexagonal and orthorhombic Nb_2O_5 for high-rate lithium ion insertion. CrystEngComm. 2016;18(14): 2532.
[32] Kim H, Lim E, Jo C, Yoon G, Hwang J, Jeong S, Lee J, Kang K. Ordered-mesoporous Nb_2O_5/carbon composite as a sodium insertion material. Nano Energy. 2015;16:62.
[33] Viet AL, Reddy MV, Jose R, Chowdari BVR, Ramakrishna S. Nanostructured Nb_2O_5 polymorphs by electrospinning for rechargeable lithium batteries. J Phys Chem C. 2010;114(1):664.
[34] Wei M, Wei K, Ichihara M, Zhou H. Nb_2O_5 nanobelts: a lithium intercalation host with large capacity and high rate capability. Electrochem Commun. 2008;10(7):980.
[35] Yang C, Yu S, Lin C, Lv F, Wu S, Yang Y, Wang W, Zhu Z-Z, Li J, Wang N, Guo S. $Cr_{0.5}Nb_{24.5}O_{62}$ nanowires with high electronic conductivity for high-rate and long-life Lithium-ion storage. ACS Nano. 2017;11(4):4217.
[36] Kong L, Zhang C, Wang J, Qiao W, Ling L, Long D. Free-standing T-Nb_2O_5/graphene composite papers with ultrahigh gravimetric/volumetric capacitance for Li-ion intercalation pseudocapacitor. ACS Nano. 2015;9(11):11200.
[37] Lyu F, Yu S, Li M, Wang Z, Nan B, Wu S, Cao L, Sun Z, Yang M, Wang W, Shang C, Lu Z. Supramolecular hydrogel directed self-assembly of C- and N-doped hollow CuO as high-performance anode materials for Li-ion batteries. Chem Commun. 2017;53(13):2138.
[38] Dylla AG, Henkelman G, Stevenson KJ. Lithium insertion in nanostructured TiO2(B) architectures. Acc Chem Res. 2013; 46(5):1104.
[39] Zeng GY, Wang H, Guo J, Cha LM, Dou YH, Ma JM. Fabrication of Nb_2O_5/C nanocomposites as a high performance anode for lithium ion battery. Chin Chem Lett. 2017;28(4):755.